VU Research Portal

Structural and spectroscopic in vivo imaging of the human retina with scanning light ophthalmoscopy

Damodaran, M.

2020

document version
Publisher's PDF, also known as Version of record

Link to publication in VU Research Portal

citation for published version (APA)
Damodaran, M. (2020). *Structural and spectroscopic in vivo imaging of the human retina with scanning light ophthalmoscopy.* [PhD-Thesis - Research and graduation internal, Vrije Universiteit Amsterdam].

3

Digital micromirror device based ophthalmoscope

based on :

M. Damodaran, K. V. Vienola, B. Braaf, K. A. Vermeer, and J. F. de Boer, "Digital micromirror device based ophthalmoscope with concentric circle scanning," Biomed. Opt. Express 8, 2766-2780 (2017).

partly based on:

K. V. Vienola, **M. Damodaran**, B. Braaf, K. A. Vermeer, and J. F. de Boer, "In vivo retinal imaging for fixational eye motion detection using a high-speed digital micromirror device (DMD)-based ophthalmoscope," Biomed. Opt. Express 9, 591-602 (2018). [section 3.5]

Abstract

Retinal imaging is demonstrated using a novel scanning light ophthalmoscope based on a digital micromirror device with 810 nm illumination. Concentric circles were used as scan patterns, which facilitated fixation by a human subject for imaging. An annular illumination was implemented in the system to reduce the background caused by corneal reflections and thereby to enhance the signal-to-noise ratio. A 1.9-fold increase in the signal-to-noise ratio was found by using an annular illumination aperture compared to a circular illumination aperture, resulting in a 5-fold increase in imaging speed and a better signal-to-noise ratio compared to our previous system. We tested the imaging performance of our system by performing non-mydriatic imaging on two subjects at a speed of 7 Hz with a maximum $20°$ (diameter) field of view. The images were shot noise limited and clearly show various anatomical features of the retina with high contrast.

3.1 Introduction

Retinal imaging is an indispensable tool for diagnosing pathologies associated with the retina. Most retinal pathologies exhibit structural and functional changes in the ocular fundus [1]. Novel methods of observing and monitoring these changes have attracted much attention. The ocular fundus is located in the posterior part of the eye is minimally reflective and moderately scattering [2–4] making imaging challenging.

Traditional fundus photography uses so-called flood illumination where a homogeneous broadband light illuminates the whole field-of-view (FOV) [5]. In this type of imaging, both the in-focus and out-of-focus light reflected from the retina is collected by the camera, where the latter reduces the image contrast. To reject the out-of-focus light, pinholes can be implemented to make the system confocal. The confocal arrangement requires scanning using a spot or a line and produces higher contrast images by rejecting out-of-focus light [6–10].

Scanning laser/light ophthalmoscopy (SLO) is used widely in clinical settings for investigation and monitoring of the retina. In a conventional confocal SLO [10–12], a single spot is used to scan the retina continuously over two dimensions using scanning mirrors. Significant improvement in speed can be achieved by eliminating one scan dimension and using a line illumination in ophthalmoscopes[13–16] at the cost of a reduced confocality.

Spatial light modulators such as a digital micromirror device (DMD) have been used for retinal imaging by projecting a series of scan patterns [17–19] without us-

ing conventional scanning mirrors. The DMD provides temporal and spatial flexibility for illumination which can have several advantages such as optimising the system for speed and confocality. To date, retinal imaging systems based on DMDs either employ a single-line scanning method combined with a camera operating in rolling shutter mode [19] or use a large number of parallel lines with a global shutter camera as reported in our prior work [17]. Muller *et al.* reported acquiring confocal images with a 38° FOV at 14.3 Hz and the registering and averaging 50 frames into a single high-quality image. Our first-generation parallel line scanning ophthalmoscope (PLSO) produced high-quality images with a 10° × 10° FOV at an imaging speed of 1.4 Hz although without averaging. At these speeds, image quality can suffer from motion artefacts, and a larger FOV is desirable.

In this paper, we present a parallel and circle SLO which uses a DMD to produce concentric circle illumination to fixate the eye and reduce eye motion during imaging. The signal-to-noise ratio (SNR) is improved by eliminating back reflections from the cornea. Corneal back reflections typically have higher intensities compared to the intensity reflected from the retina and reduce the image quality by forming a de-focussed background in the image. An annulus is placed conjugate to the pupil plane to create an annular illumination, and the reflected light from the retina is collected through the un-illuminated portion in the centre [20]. A circular aperture in the detection arm blocked most of the corneal reflections but passed the signal from the retina to the camera. The resulting improvement in SNR enabled faster imaging speeds without reducing the image quality.

A model eye was developed to study the SNR improvement obtained with the annulus and a circular aperture with the same outer diameter. Imaging two healthy volunteers demonstrated the capability of the system for *in vivo* retinal imaging.

3.2 Methods

The study obeyed the principles of the Declaration of Helsinki and was approved by the Institutional Review Board for human use at the VU University medical centre, Amsterdam. A written, informed consent was obtained from each subject. The optical power used for measuring human subjects was in agreement with the maximum permissible exposure limit prescribed by the latest IEC standard 60825-1 [21].

3.2.1 Optical system

The optical layout of the system is shown in Fig. 5.3A. A light-emitting diode (LED) with a bandwidth of 30 nm and a centre wavelength of 810 nm (SFH 4780S, OSRAM GmbH, Munich, Germany) was used for illumination. The half-angle divergence of the LED was $\pm 10°$ with a maximum radiant intensity of 2900 mW/sr. The use of a LED with low spectral coherence reduced the speckle noise in the final retinal images. The light from the LED was homogenised using a tapered light pipe homogenising rod (Edmund Optics Inc., Barrington, USA) with a square entrance aperture (4 mm $\times$ 4 mm). The lenses L1 (f = 40 mm) and L2 (f = 50 mm) relayed the exit aperture (8 mm $\times$ 8 mm) of the light pipe onto the DMD.

The SLO used a DMD with a 0.7-inch diagonal micromirror array containing 1024 $\times$ 768 micromirror elements with a pitch of 13.6 ţm. The Vialux™ DLP©V-module V4100 board (Vialux GmbH, Chemnitz, Germany) provided control logic and power for the DMD. Each micromirror can be individually programmed to be in an 'ON' or 'OFF' state. A total internal reflection (TIR) prism [22] was used to guide the reflected light from the micromirrors in a perpendicular direction. The 4f system consisting of the lens pairs L3 (f = 37.5 mm), L4 (f = 42.9 mm), the ophthalmic lens L5 (f = 30 mm) and the eye (f = 60 D or 16.7 mm for a typical eye) relayed the light reflected from the DMD 'ON' mirrors onto conjugate positions on the retina. The DMD was magnified by a factor of 0.64 and illuminated the retina with a FOV of 30° $\times$ 21°. The scattered and reflected light from the retina was imaged on the CMOS camera (ace2040-180kmNIR, Basler, Germany) using lens L6 (f = 40 mm) and the camera objective lens L7 (f = 16 mm). The retinal image was magnified by a factor of 0.72 on the camera, forming an image of approximately 1150 $\times$ 850 pixels. However, due to the aberrations and field curvature induced by the optics, the maximum area where the retina was in sharp focus corresponded to a FOV of 20° diameter. Overall, the DMD was magnified by a factor of 0.45 onto the camera plane. Individually, each DMD mirror element was mapped to 1.1 pixels in the camera.

To minimise the stray reflections from the optical elements in the system, we used polarizers P1 and P2 in cross-polarized states in combination with the polarizing beam splitter (PBS) and the quarter-wave plate (QWP). The light from the DMD was linearly polarised to the transmission state of the PBS after passing through P1 and was then circularly polarised after passing through the QWP. The reflection from the retina (and the cornea) again passed through the QWP in the return path, which converted the reflected light to a linear polarisation state aligned with the reflection state of the PBS and passed through P2. In this configuration, the stray
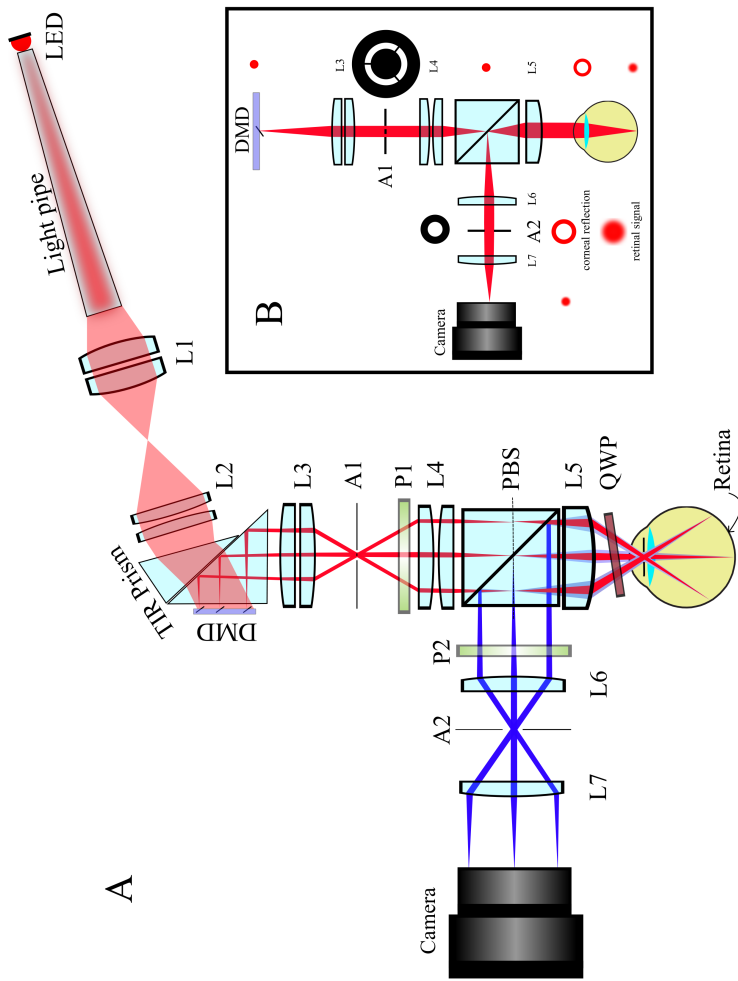
Figure 3.1: A: Schematic of the optical setup showing both the illumination path (red) and the reflection path (blue). L1-L7: Lenses; P1, P2: Polarisers; A1: Annulus; A2: Circular aperture; PBS: Polarizing Beam Splitter; QWP: Quarter Wave Plate. B: The optical paths and beam shapes at different positions in the setup to block the corneal reflections - A point source in the DMD was relayed to a point in the retina using a 4f system consisting of lenses L3-L5 and the eye lens. An annulus was placed at the conjugate pupil plane between lenses L3 and L4 and was imaged onto the cornea using L4 and L5. The reflection from the retina was relayed to the camera using another 4f system consisting of the eye lens and the lenses L5-L7. The reflection from the cornea formed an image again at the conjugate pupil plane in the detection arm and was blocked by the circular aperture, while the retinal signal passed through the circular aperture.

reflections by components in the system between the two cross polarisers were rejected.

The camera sensor contained 2048 × 2048 pixels on a 5.5 µm pitch and operated in a global shutter mode. The maximum frame rate at full resolution was 180 frames/second (with 8-bit encoding). The full well charge of each pixel was 11800 electrons (e). A frame grabber (NI PCIe-1473R, National Instruments Inc., USA) was used to acquire and save images. The DMD control board sent the trigger signals to the camera to capture a frame for each pattern. There was a live preview of the image acquired by the camera to make sure that the retina is in focus in the camera.

3.2.2 Annular illumination on the pupil plane and retinal resolution

The diameter of a un-dilated pupil varies according to factors such as age and the luminance of the light used for imaging. The system was designed for a 3 mm pupil diameter as it corresponds to the diameter of an undilated pupil reported in the literature [23]. An annulus with an outer diameter of 4 mm and an inner diameter of 3 mm was made by laser cutting a 1 mm thick sheet of metal. The central obstruction is connected to the outer obstruction by thin metal bridges, as shown in Fig. 5.3B. The annulus was placed conjugate to the pupil plane (A1 in Fig. 5.3B) between L3 and L4 to create an annular illumination on the cornea with an outer diameter of 2.8 mm and an inner diameter of 2.1 mm. The image of the annular corneal reflections is focussed at the conjugate plane in the detection arm at location A2 in Fig. 5.3B and has an outer diameter of 3.7 mm and an inner diameter of 2.8 mm. We used a 2.8 mm circular aperture in the detection arm to block the corneal reflections and allow imaging the retina through the central un-illuminated portion of the pupil [20]. Thus, we rejected most of the corneal reflections and reduced the background, thereby improving the SNR. Having a circular aperture of 2.8 mm diameter in the detection arm translates to a 2.1 mm circular aperture on the cornea. From the Rayleigh criterion, this corresponds to a resolution of 7.9 µm on the retina and 5.6 µm in the camera plane. Since the camera pixel size was 5.5 µm, the resolution was not limited by the camera. In practice, the resolution in the retina is worse because of ocular aberrations. For the measurements on the model eye with an aperture, the annulus was replaced by a circular aperture with a diameter of 3 mm.

3.2.3 Parallel scanning method

The DMD can be used to create a large variety of parallel scanning patterns, as shown in Fig. 3.2. The illumination pattern is produced by programming sequential binary patterns which are displaced relative to each other by a constant distance. The parallel scanning strategy has already been showed to provide high-quality confocal images in fluorescence microscopy [24, 25]. The parallel line scanning ophthalmoscope (PLSO) [17] has been used to produce *in vivo* retinal images.

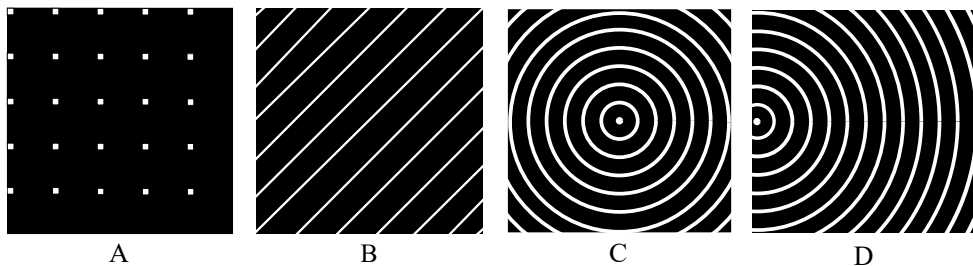|			
A	B	C	D

Figure 3.2: Illustrations of the parallel scanning methods used - A: Spots have been used in fluorescence microscopy for imaging stationary biological samples [24]. B: Parallel lines used in our prior work (PLSO) [17]. C: Concentric circles used in our system for scanning with the centres of the circles in the middle of the frame. D: Concentric circle scanning with the centre of the circles at the edge of the frame

However, there is a natural tendency for the human eye to follow motion, in this case, the moving spot (Fig. 3.2A) or line (Fig. 3.2B) patterns which are projected typically at 100 Hz to 200Hz. This eye movement caused by the subjects inclination to follow the scan patterns leads to motion artefacts in the final images. However, a pattern of concentric circles that shrink provides an illusion of depth where the subject tends to fixate on the centre of the concentric circles where each circle seems to disappear. When the circles are centred in the middle of the DMD (Fig. 3.2C), the fovea is in the middle of the FOV. When the centre of the circles is shifted to different regions on the DMD, *e.g.* the edge of the DMD (Fig. 3.2D), the subject fixates on the centre of these circles bringing different areas around the fovea in the FOV, including the optic nerve head (ONH). Thus, an area around the fovea can be imaged with a scan pattern that at the same time, provides a fixation target to the subject.

Each mirror in the DMD can be programmed individually to be turned 'ON', thereby reflecting the light along the optic axis or turned 'OFF' thus not contributing to the illumination on the retina. Let s be the number of 'ON' mirrors per scanning pattern and p be the total number of DMD mirrors used for illumination. The fill-factor (Γ) for scanning the retina is then defined as

$$\Gamma = \frac{s}{p}. \tag{3.1}$$

$N = 1/\Gamma$ then gives the total number of patterns required for scanning the FOV. At the end of N measurements, we have an image stack of N frames. By summing all the frames into a single image, we obtain a wide-field image.

3.2.4 Confocal image processing using virtual pinholes

True confocality occurs in an ophthalmoscope which has an illumination pinhole to produce a diffraction-limited spot in the retina and a detection pinhole which suppresses the out-of-focus scattered light. Line scanning achieves quasi confocality, not all out of focus light is rejected. Some of the scattered light from adjacent illuminated spots along the line dimension can lead to cross talk in the image. This is also true for parallel illumination schemes such as multiple lines or concentric circles. To create a confocal image, pinholes should be implemented in the detection arm. These pinholes should be precisely position matched with the illumination pattern to extract just the signal reflected from the sample and reject the out-of-focus light. These detection pinholes are tough to implement as real physical pinholes, and hence these pinholes ought to be created in the digital domain using post-processing techniques.

To reduce the scattered light from the retina and suppress the corneal reflections for each pattern in the sequence, we used a post-processing method first presented by Heintzmann *et al*. [26]. The Heintzmann method determines the maximum and minimum greyscale values for every image pixel overall acquired pattern frames (I). The maximum value corresponds to the signal in focus, while the minimum value is a measure of the background signal. The values in between the maximum and minimum relate to different amounts of out-of-focus signal and are therefore excluded from the analysis. The confocal image $I_{conf}(x, y)$ is then calculated as the difference between the maximum and the minimum pixel values as:

$$I_{conf}(x, y) = \max_{i=1..N}[I(x, y; i)] - \min_{i=1..N}[I(x, y; i)]. \tag{3.2}$$

In this study, the five lowest values per pixel were averaged to obtain a better estimate of the background value for each pixel, and this value was subtracted from the maximum value of that pixel.

3.2.5 Model eye measurements to evaluate SNR improvement

In this section, we describe the SNR model and the experiments done in the model eye to evaluate the SNR improvement with an annulus compared to a circular aperture for different fill-factors. These experiments demonstrate the SNR in the transitional regime between point scanning and full-field illumination and form the rationale behind the increase in imaging speed with the annulus without compromising the SNR. A model eye was developed to characterise the imaging performance and to study the SNR improvement when using a circular aperture or an annulus. An uncoated N-BK7 0.5-inch plano-convex lens with a 15 mm focal length (LA1540, Thorlabs GmbH, Germany) and a 7.7 mm radius of curvature was used in the model eye. This radius of curvature matched well to the human cornea anterior radius of curvature of approximately 7.6 mm [27]. The near-identical radius of curvature in the model eye ensured that the corneal reflections for the model eye followed the same ray paths as can be expected for the human eye. Besides, the model eye was filled with water to mimic the optical properties of the human eye, which increased the focal length to 20 mm. A uniformly scattering layer of titanium dioxide (TiO_2) of 300 µm thickness and scattering coefficient (μ_s) of 10 mm^{-1} was used as an artificial retina. The amount of power incident on the DMD remained constant as a function of fill-factor but varied between two values for the annulus and aperture measurement such that the power incident on the cornea was the same for annulus and aperture with the same fill-factor. As a result, the amount of optical power incident on the cornea (180 µW at $\Gamma = 0.05$) varied with the fill-factor Γ only for both the annulus and aperture measurements.

We determined the readout and dark noise variance for the camera by taking dark frames. The dark plus read-out noise power ($\sigma^2_{dark+readout}$) was approximately 350 e^2. We further determined the step size of the A/D conversion by illuminating the sensor with different power levels, establishing the gain factor according to the European Machine Vision Association (EMVA) standard [28] as shown in Fig. 3, which gave a step size of 46 electrons per digital number (DN). The quantization noise then becomes $(46)^2/12 = 176$ e^2. The total measured noise of 350 e^2 minus the quantization noise of 176 e^2 results in a dark noise power of 174 e^2. Therefore, the shot noise limited regime is reached above 350 detected photoelectrons or a digital number DN = 7.5. Our retinal measurements were performed at detection levels of 2500 photoelectrons (DN = 54).

We took the following definition of SNR according to the European Machine Vision Association standard [28]:
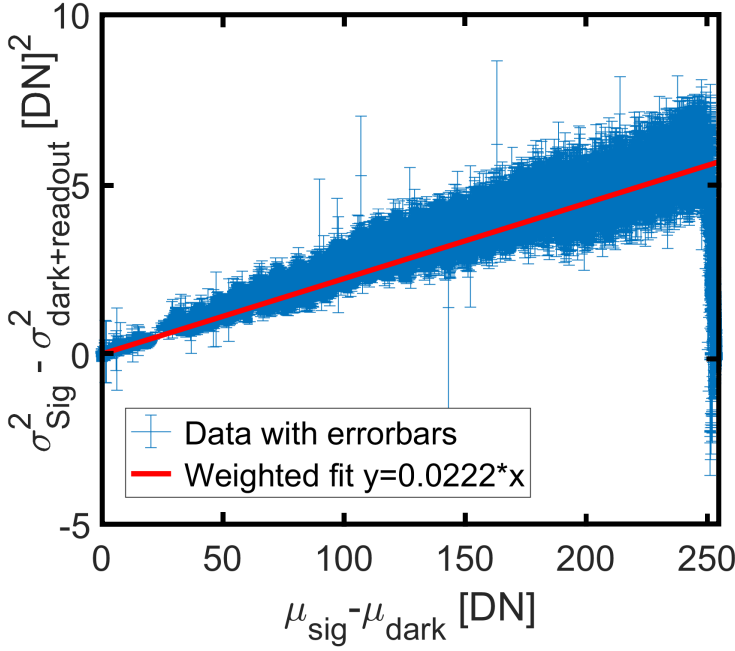
Figure 3.3: The measured variance $\sigma_{sig}^2 - \sigma_{dark+readout}^2$ against the mean gray value $\mu_{sig} - \mu_{dark}$ and the linear regression line used to determine the overall system gain K. σ_{sig}^2 is the variance in signal and μ_{sig} is the mean signal. The graph indicated that the gain of the system is 46 electrons/ DN (1/ slope of the fitted line) according to the method described in the EMVA standard [28].

$$SNR(\mu_p) = \frac{\eta\mu_p}{\sqrt{\sigma_d^2 + \sigma_q^2/K^2 + \eta\mu_p}} \tag{3.3}$$

where η is the wavelength-dependent quantum efficiency of the camera sensor, μ_p is the mean photon count, K is the overall system gain and σ_d and σ_q are the dark noise and quantization noise respectively. In our system, dark noise and quantum noise were negligible for the signal levels we obtain on the camera and hence Eq. (3.3) becomes,

$$SNR_s = \frac{\eta\mu_p}{\sqrt{\eta\mu_p}} = \frac{\mu_e}{\sqrt{\mu_e}} \tag{3.4}$$

where μ_e is the mean number of electrons. Based on the encoding, the number of electrons is converted to a grey value by the camera. These values have contributions both from the light reflected from the retina (retinal signal) and the light reflected from cornea and other surfaces. If $\mu_{e,background}$ is the background and $\mu_{e,signal}$ is the total signal on the camera, the light reflected exclusively from the
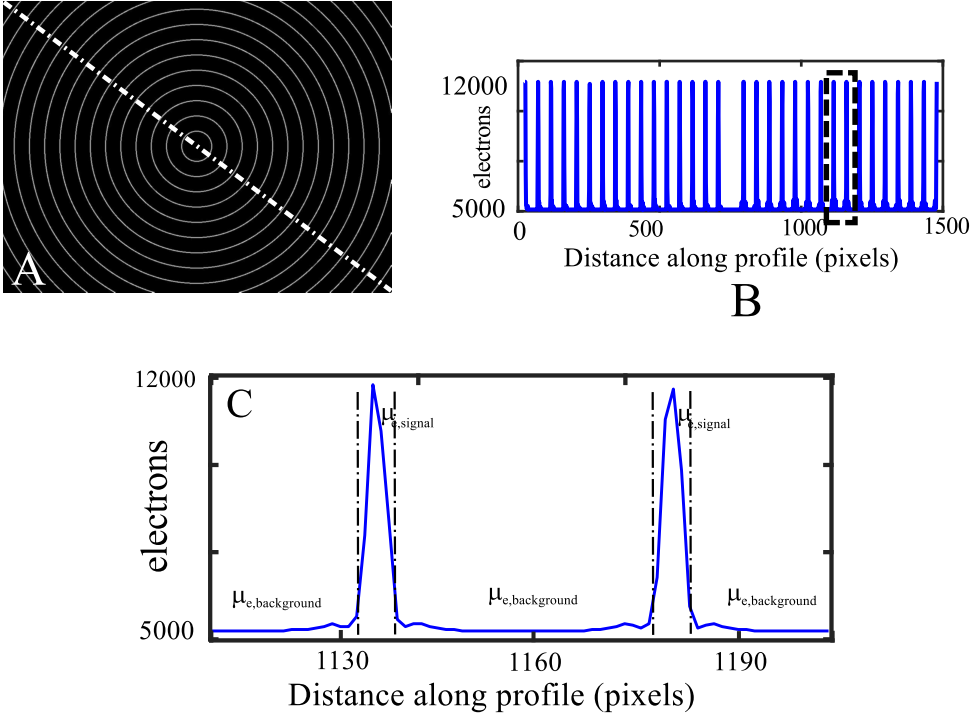
Figure 3.4: Calculating the SNR - illustration : A single frame from the stack of images (Γ = 0.05 illustrated here) is taken and a line profile is plotted (shown as white line). B: The line profile along the white line showing peaks along the signal. C: Each peak is examined to estimate $\mu_{e,signal}$ and $\mu_{e,background}$. This is repeated for several line profiles and the averages of $\mu_{e,signal}$ and $\mu_{e,background}$ is recorded.

retina is given by $\mu_{e,signal} - \mu_{e,background}$. Then the SNR for the retinal signal alone (SNR_s) can be rewritten as [17]

$$SNR_s = \frac{\mu_{e,signal} - \mu_{e,background}}{\sqrt{\mu_{e,signal}}} \tag{3.5}$$

The retinal signal per pixel remains constant for all values of Γ. However, the total background varies linearly with Γ. Eq. (3.5) can then be written as:

$$SNR_s(\Gamma) = \frac{\alpha}{\sqrt{\alpha + \beta \cdot \Gamma}} \tag{3.6}$$

with α the retinal signal ($\mu_{e,signal} - \mu_{e,background}$) per pixel and β the background per pixel. Equation (3.6) was used as a model to fit the experimental SNR_s data. The SNR_s for the annulus and the circular aperture as described in section 3.2.2 was measured for different Γ. When a circular aperture was used, the corneal reflections saturated the camera. Reducing the source power below the saturation threshold

gave a very poor signal with the annulus. Hence a neutral density (ND) filter (OD = 0.6, 35% transmission at 810 nm) was placed in front of the camera when measuring with the circular aperture to prevent saturation. The mean electron count was corrected for this attenuation.

The SNR_s was estimated for different Γ with the DMD projecting patterns at 140 Hz. For each Γ, one frame (Fig. 3.4A) was taken, and the signal profile was plotted along different lines, as illustrated in Fig. 3.4B. The mean signal was estimated within a $1/e^2$ width of the signal peak and the mean background was measured elsewhere from this profile as shown in the Fig. 3.4C. The same procedure was repeated several times and averaged.

3.2.6 *In vivo* retinal imaging

To demonstrate the imaging capabilities of our system, we imaged the right eye of two healthy volunteers. Subject 1 was 32 years old with a refractive error > -1 D and subject 2 was 27 years old with a refractive error > -1.75 D and astigmatism of -2.25 D. Imaging was performed in a dimly lit room with un-dilated pupils ($\sim$ 3 mm in diameter) and with an incident power at the cornea of 180 ţW. The maximum permissible radiant power for a collimated static beam at 810 nm wavelength is 639 ţW [21]. Laser safety calculations are detailed in the Appendix.

The DMD was used to project concentric circular pattern at 140 Hz with a Γ = 0.05 (N = 20) resulting in an imaging speed of 7 Hz. An annulus with dimensions as described in section 2.2 was used to minimise the corneal reflections. The circular pattern stimulated the subject to fixate on the centre of the circular design. The ophthalmic lens could be translated along the optic axis to bring the retina in focus. The measurements were done for 7.2 seconds (1000 frames). Confocal videos were created by updating the image stack with every newly acquired pattern frame and recalculation of the confocal image. As such out of a single dataset, a confocal video with 981 video frames could be obtained.

3.3 Results

3.3.1 Model eye measurements to evaluate SNR improvement

Figure 3.5A shows the mean signal (retinal signal + background) and mean background plotted for different values of Γ for both the circular aperture and the annulus. When the Γ increases, so do the background and the low signal. The offset

between these two is the retinal signal which remains constant with both illumination methods.
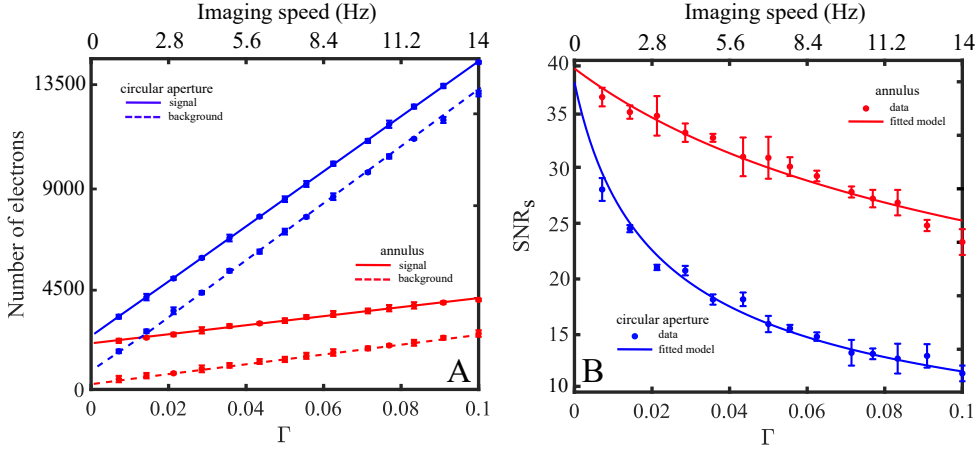

Figure 3.5: A: The signal and background obtained in the model eye for different imaging speeds. Blue and red lines and points are for the circular aperture and annulus, respectively. B: SNR comparison obtained in the model eye with the annulus and aperture for different imaging speeds. The imaging speed indicated in the top horizontal axis is for a DMD pattern speed of 140 Hz.

As explained in section 3.2.2, the corneal reflections which form as a background in the image are substantially reduced with the annulus. The SNR_s model (Eq. (3.6)) was used to fit the SNR_s data for different values of Γ. For the circular aperture, the model fit gave α = 1499 e and β = 134645 e. For the annulus, the model fit gave α = 1531 e and β = 20344 e. These values are in agreement with the argument that the retinal signal α remains fairly constant for both circular aperture and the annulus for the same power level on the cornea. At the same time, there is a 6.6-fold decrease in the background when an annulus is used. This effect translates to increase in SNR_s as shown in Fig. 3.5B.

When the Γ is as small as possible (for example only one mirror on at a time), the performance of the system falls in line with a conventional single spot scanning SLO. Then the SNR_s should be the same with or without annulus, as the corneal reflections would be minimal also in circular illumination case. This effect is already seen in Fig. 3.5B as the curves start to converge for small values of Γ. However, for Γ>0.4, the benefit of using an annulus is pronounced as there is almost a two-fold increase (1.9 at Γ=0.05) in the SNR_s. It is also evident from Fig. 3.5B that a given SNR_s can be achieved for a higher fill-factor Γ in the case of an annulus compared to a circular aperture thereby making higher imaging speeds feasible in terms of SNR.

There was still some background when the annulus was used for imaging. This residual background can be attributed to light scattering in the retina, which contributes to the background and some small portion of the corneal reflection which reaches the camera. Further, the image formed by a single DMD mirror projected on the retina through an annulus is convolved with the system optics point spread function of the circular aperture in the detection arm to form a slightly blurred spot on the camera. Also, when the corneal reflections are defocused at the circular aperture in the detection arm, they do not get blocked completely.

3.3.2   *In vivo* retinal images

Figure 3.6 shows the results of in vivo imaging of the foveal region and various peri- and parafoveal regions around the retina of subject 1. Figure 3.6A is a fundus photograph (Canon CR-2, Canon Europa N.V, The Netherlands) with the coloured circles highlighting the different peri- and parafoveal regions with the fovea in the centre (blue dashed circle). Since we used polarization optics in our system, the macular bow-tie structure is noticeable in Fig. 3.6D. This structure occurs around the fovea due to a meridional variation in birefringence exhibited by Henle's fibres surrounding the fovea [29]. The different regions (Figs. 3.6B-3.6G) were imaged with a 18° FOV (diameter) by shifting the centre of the concentric circles to different places in the DMD.

Figure 3.7 shows the comparison of a *in vivo* image with a Spectralis (Heidelberg Engineering GmbH, Heidelberg, Germany) confocal SLO image of the inferior region of the retina of subject 1. Figure 3.7A is the non-confocal image produced by adding all the individual frames. This image suffers from multiple scattered and out-of-focus light resulting in poor quality with features that are not discernible. The virtual pinholes method was applied to this image in Fig. 3.7B, which shows the resulting high contrast confocal image. Figure 3.7C shows the average of 5 confocal frames after median filtering with a kernel of 3×3. Figure 3.7D and Figure 3.7E show the single frame and 20 frame average from a Spectralis SLO using the infrared (IR) channel. Figure 3.7F shows the line profiles through the same blood vessels (indicated by numbers 1 through 5 in Fig. 3.7B) from the images shown in Figs. 3.7A-3.7E. Arrows indicate the location of 5 blood vessels. The single-frame Spectralis SLO shows a marginally better Michelson contrast ([max-min/max+min]) for blood vessel 5 compared to the single frame DMD based SLO (0.52 vs 0.47), while the contrast for the blood vessel 2 (smallest) is better with the DMD based SLO (0.31 vs 0.25).
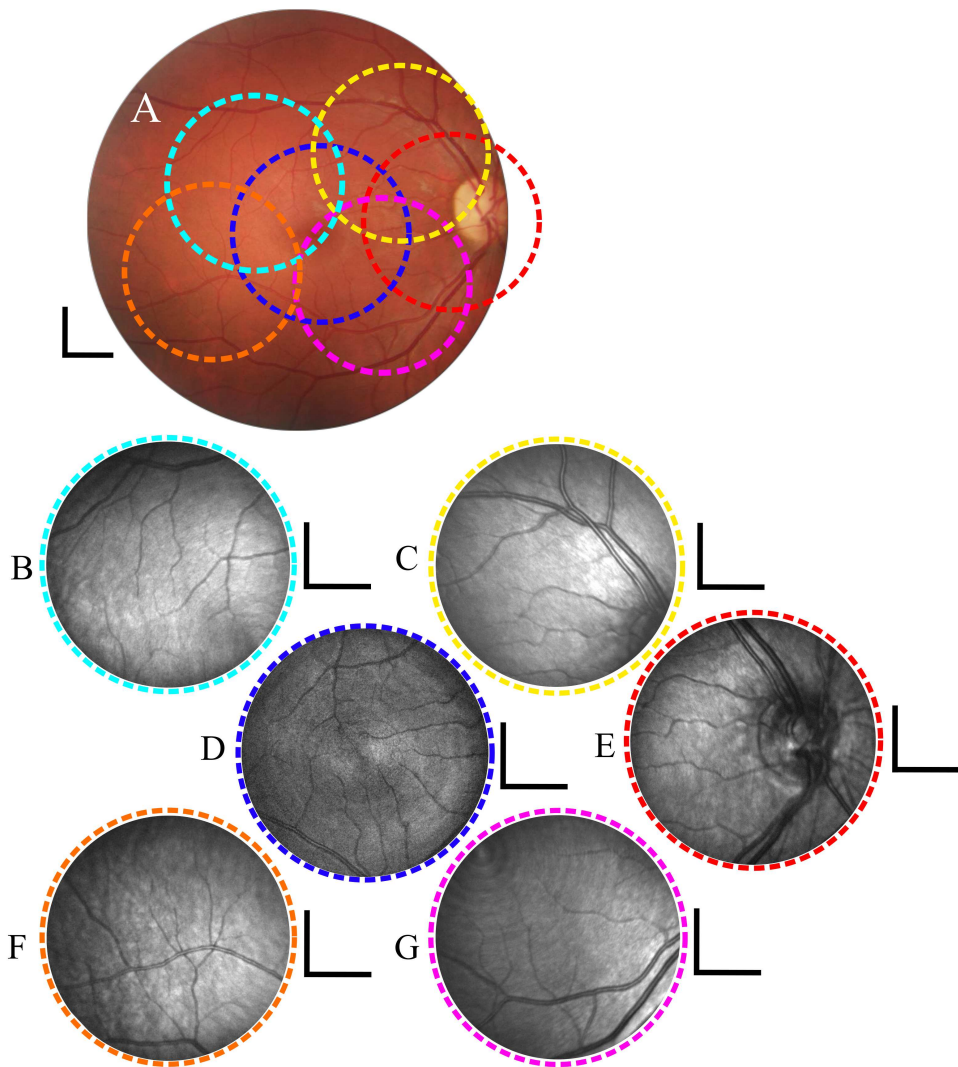
Figure 3.6: A: Fundus photograph of subject 1 coloured dashed circles showing the area imaged with our system. B-G: confocal images of the corresponding region showing the fovea and various peri- and parafoveal regions. Scale bar is 2° in the retina.

Figure 3.8 shows the *in vivo* results of different regions of the retina of subject 2 by projecting concentric circles with centres at two different locations in the DMD. Figure 3.8A shows the fundus photograph (Topcon TRC 50-DX Type 1A, Topcon Europe Medical B.V., The Netherlands) of subject 2 with a 50° FOV with the regions imaged with our system denoted by dashed circles. Figure 3.8B shows the macular region with fovea in the centre (red arrow) with a 20 degree FOV. Figure 3.8C shows the image of the optic nerve head.
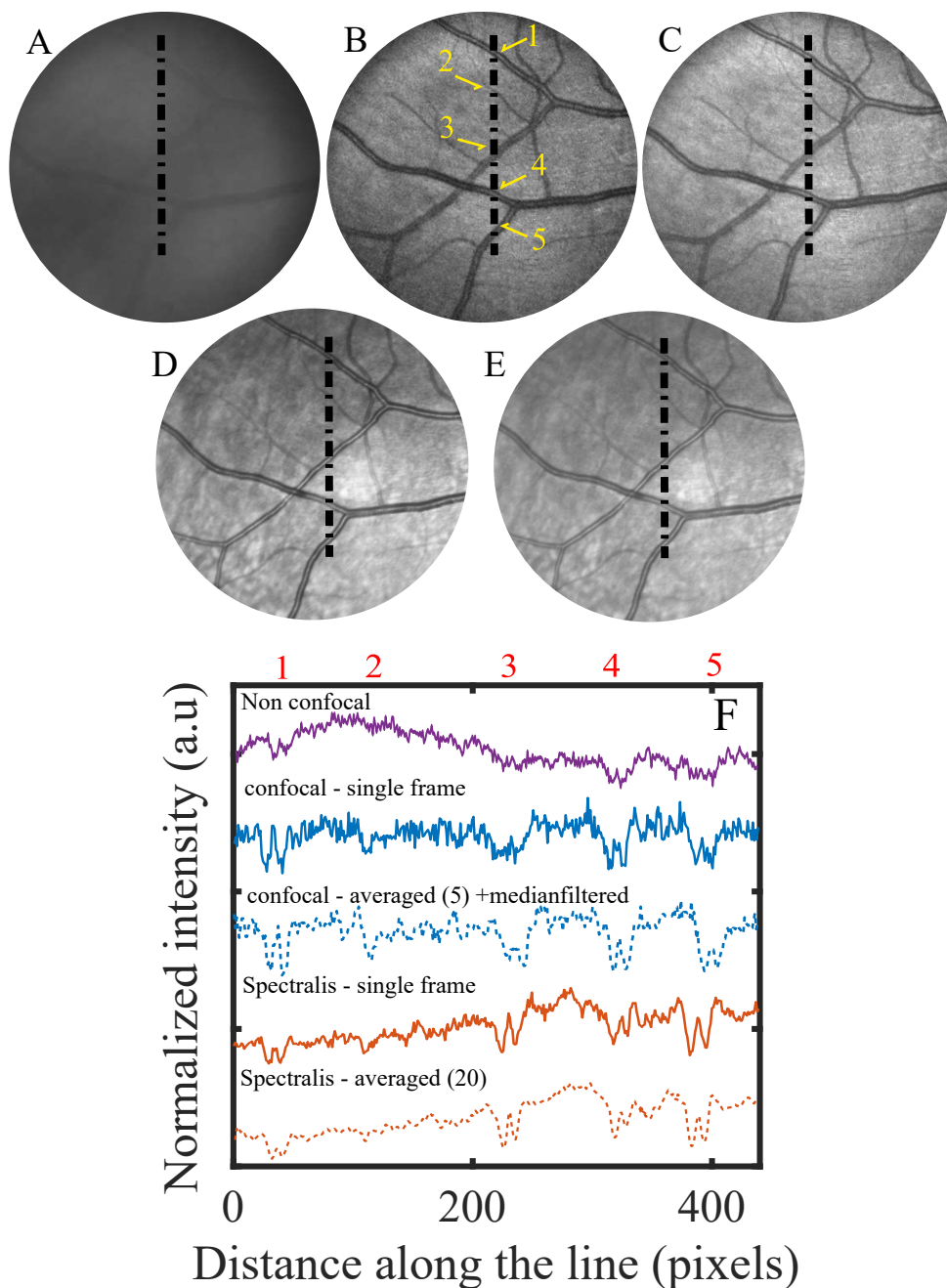
Figure 3.7: Comparison of the DMD based SLO with a Spectralis SLO - A: Non-confocal image of the inferior region of subject 1. B: Single confocal frame from the DMD based SLO. C: 5 frame average and median filtered image from the DMD based SLO. D and E: Single frame and 20 frames averaged images from the Spectralis SLO. F: Line profiles through the line indicated in A-E crossing through five blood vessels 1-5. The location of the blood vessels is indicated in the top axis. All in-vivo images have a 16.5° FOV.
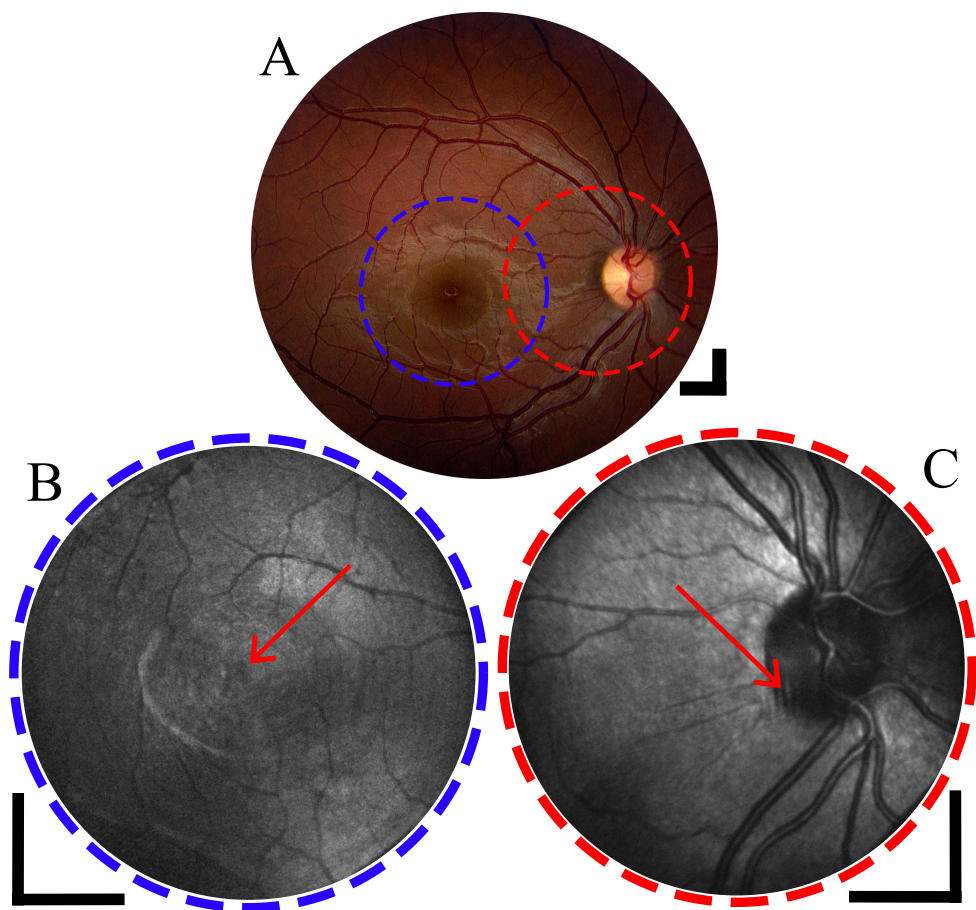
Figure 3.8: A: Fundus photograph of subject 2 showing the macular region (blue dashed circle) and the ONH region (red dashed circle) of the ocular fundus. B: The macular region with fovea indicated by the red arrow. C: The ONH (indicated by red arrow) with blood vessels surrounding it. Scale bar is 5° in the retina.

3.4 Discussion

The presented imaging device replaces scanning mirrors and laser sources that are present in the prevailing retinal scanning systems with a DMD and LEDs, potentially reducing cost and increasing flexibility. The new DMD based ophthalmoscope demonstrates several improvements over our previous method [17]. The background from corneal reflections was decreased significantly with the use of annulus, which increased the SNR by almost a factor of two. Moreover, the reduced corneal background made it possible to use higher fill-factors in the DMD, thus improving the imaging speed of the system from 1.4 Hz to 7 Hz without any loss in SNR. Although the concept of annular illumination has been well known for many years, this paper offers a quantitative analysis of the benefit of such lighting when going from the low fill-factor regime (conventional confocal SLO) towards flood illumination. The images obtained with our system are comparable images captured with a commercial SLO. Shifting the centre of the concentric circles to image different regions is a novel way to provide fixation while imaging different peri and parafoveal regions.

The system is modular with respect to the light source and enables changing the wavelength for imaging. Adding new wavelengths will make the system achieve multi-spectral imaging. Multi-spectral retinal imaging has gained interest in recent years [30, 31] as it helps to gather quantitative information on retinal health. The *in vivo* images sometimes show faint circular artefacts after post-processing. This is attributed to motion artefacts creating a discontinuity in scanning. It could be possible to extract motion information and use this to track the eyes movement. When done fast enough, it will also enable doing eye motion correction in real-time [32, 33] to improve the quality of the images by averaging multiple images at the same location and correct for the minor motion artefacts present in these images. Image registration could potentially be better with the parallel illumination as all the illumination points of a single frame are undistorted.

The primary shortcoming of the system is that the illumination light efficiency is poor. The DMD is operated at low fill-factor resulting in the majority of power not being used. Hence a high power and low divergence LED is needed to provide sufficient power for imaging the retina. Although a low divergence LED was used in our system, this might not be available for all wavelengths, particularly for the wavelengths of interest for multispectral imaging. This is expected to improve in the future with the progress in LED source development. As we currently are a factor of 4 below the maximum permissible exposure according to the IEC standard 60825-1 [21], there is still considerable room for further improvement. The polariza-

tion optics to reduce the stray reflections in the system lead to polarisation artefacts in the images due to birefringence of the cornea [34] and retina [29], influencing the images being recorded.

The position of the cornea in the imaging system is critical for the annulus to provide complete rejection of the corneal reflections. If the cornea is not positioned in the optimal imaging plane, the corneal reflections are not blocked, and hence they reach the camera. Although the subjects head is placed on a chin rest, small movement can occur. A pupil camera which tracks the location of the beam on the cornea can be implemented, allowing the re-positioning of the illuminating beam to the centre of the cornea.

3.5 Application: Fixational eye motion detection

As an application of the DMD based ophthalmoscope [35, 36], Retinal motion detection with an accuracy of 0.77 arcmins corresponding to 3.7 μm on the retina was demonstrated. The sub-sampled frames provide 7.7-millisecond snapshots of the retina without motion artefacts between the image points of the subsampled frame, distributed over the full field of view. An ophthalmoscope pattern projection speed of 130 Hz enabled a motion detection bandwidth of 65 Hz. A model eye with a scanning mirror was built to test the performance of the motion detection algorithm. Furthermore, an in vivo motion trace was obtained from a healthy volunteer. The captured eye motion trace clearly shows the three main types of fixational eye movements (FEM). Lastly, the obtained eye motion trace was used to correct for the eye motion in consecutively obtained subsampled frames to produce an averaged confocal image correct for motion artefacts.

In vivo eye motion detection

An example of an in vivo image correlation [35] is shown in Fig. 3.9. The reference, in this case, is a confocal image of the ONH area. The subsampled frame of the same area is then cross-correlated with the reference frame resulting in a 2D correlation matrix seen on the right side of Fig. 3.9. With the 5% fill factor of the DMD, the highest normalized cross-correlation coefficient values reach about 0.3 to 0.35. For the *in vivo* data we did not determine the centre of mass of the cross-correlation, but used the peak location, resulting in a motion resolution determined by the image pixel size (corresponding to 7.9 μm on the retina or 1.6 arcmins).

An *in vivo* eye motion trace is presented in Fig. 3.9, where the red line indicates motion in the horizontal direction and the blue trace shows motion in the vertical
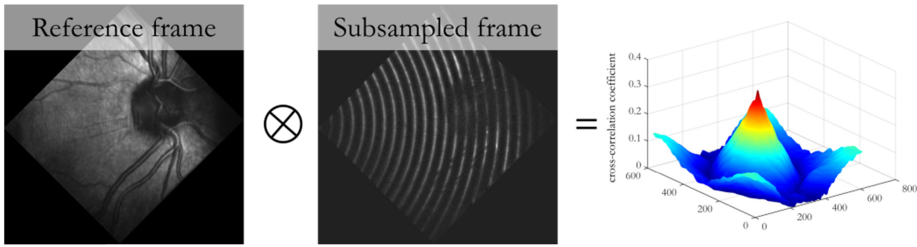
Figure 3.9: An *in vivo* example of the cross-correlation. First, a confocal frame is constructed, which will act as a reference frame. Then the next subsampled frame will be cross-correlated to the reference frame to obtain the shift between these two frames. The peak that occurs in the correlation matrix indicates the offset of the subsampled pattern with respect to the reference. The better the two images match, the higher the peak in the correlation matrix will be.

direction. All three types of FEM can be distinguished from the trace. Two microsaccades occurred during the recording at around 1.1 seconds and 2.9 seconds, having amplitudes of about 17 and 22 arcmins respectively. Slow drift is visible throughout the trace having amplitude values between 5 and 20 arcmins, which is similar to values reported in the literature [37]. And finally, the tremor is superimposed on top of the motion trace as high-frequency, low amplitude jitter.
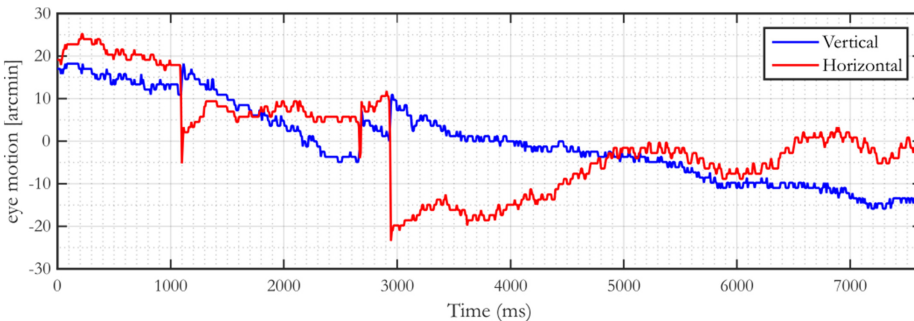

Figure 3.10: Extracted eye motion traces from a healthy subject. All three types of eye movements can be distinguished from the traces, namely micro-saccades (large jumps at 1.1 s and 2.9 s), drift (drifting motion along the trace with small amplitude and frequency) and tremor, high-frequency motion superimposed on top of the eye motion trace

The obtained eye motion trace shows the displacement of each subsampled frame compared to the reference frame. This displacement information can be used to adjust the position of each subsampled frame with respect to the reference frame and generate an averaged confocal image that is corrected for motion. For this specific data set, a total of 1000 subsampled frames were taken. With a DMD fill

factor of 0.05, this results in 50 full confocal images (20 patterns per confocal image) over 7.6 seconds with most of them affected by eye movements. Figure 3.11
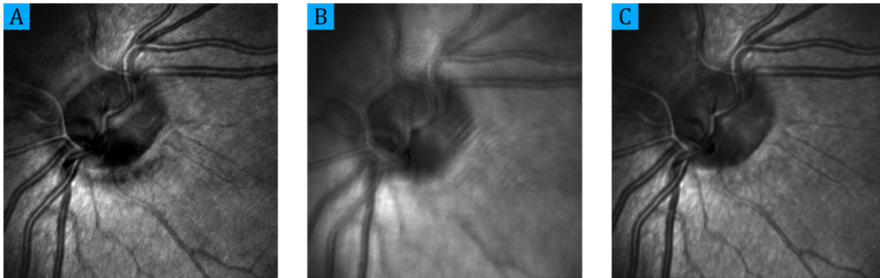

Figure 3.11: Averaging multiple confocal images without and with motion correction. To generate the images, 1000 subsampled frames were taken over 7.6 seconds. As the fill factor of the DMD was 0.05, it took 20 patterns to scan the entire FOV. This then resulted in 50 full confocal images that were averaged. (A) A single confocal image for comparison. (B) When the subsamples images are not corrected for motion, the resulting averaged image is blurry. (C) When each subsampled frame is corrected for the eye movements, the averaged image has high quality, showing good contrast and lots of features typical of the area around the ONH.

shows three confocal images. In Fig. 3.11(A), a single confocal image, is shown as a reference. In Fig. 3.11(B) the patterns are not corrected according to the eye motion trace before applying the Heintzmann algorithm, and the resulting confocal image is blurry and distorted by the eye motion. In Fig. 3.11(C), the eye movements during the measurement has been corrected before applying the algorithm. The resulting high-quality image shows good contrast and many anatomical features such as the larger blood vessels that are now sharp and the smaller vessels originating from ONH that are visible.

3.6 Conclusion

We have developed an SLO using a DMD displaying concentric circle pattern to scan the retina and provide a fixation target to the subject to fixate the eye. By changing the centre of the concentric circle pattern, different regions could be imaged. We used an annulus in the illumination arm to create an annular illumination on the cornea and block most of the corneal reflections using a circular aperture in the detection arm. Using the annulus, there was a 6.6-fold decrease in the background translating to a 1.9-fold increase in the SNR. This translates to a nearly 7-fold increase in speed for $\Gamma = 0.05$ at the same SNR. We demonstrated the experimental implementation of the imaging system by imaging two subjects in vivo with

a maximum FOV of 20° diameter at a 140 Hz sub-frame rate and 7 Hz full frame rate. Further, we have demonstrated the feasibility of eye motion detection in our DMD based ophthalmoscope. The motion detection bandwidth was 65 Hz which was enough to detect most of the eye movements in the data set. The motion detection accuracy was better than 0.77 arcmins in vivo corresponding to 3.7 μm on the retina.

References

[1] A. E. Elsner, A. H. Jalkh, and J. J. Weiter, "New devices in retinal imaging and functional evaluation," *Practical Atlas of Retinal Disease and Therapy*, W. Freeman, ed. pp. 19-35, Raven Press, New York (1993).

[2] F. C. Delori, and K. P. Pflibsen, "Spectral reflectance of the human ocular fundus," Appl. Opt. **28**(6), 1061-1077 (1989).

[3] M. Hammer, and D. Schweitzer, "Quantitative reflection spectroscopy at the human ocular fundus," Phys. Med. Biol. **47**(2), 179-191 (2002).

[4] D. A. Atchison and G. Smith, *"Optics of the Human Eye"*, Butterworth-Heinemann, pp. 34-35 Oxford (2000).

[5] R. Klein, B. E. Klein, M. W. Neider, L. D. Hubbard, S. M. Meuer and R. J. Brothers, Diabetic Retinopathy as detected using ophthalmoscopy, a Nonmydriatic camera and a standard fundus camera, Ophthalmology **92**(2), 485-491 (1985) .

[6] R. H. Webb, G. W. Hughes, and O. Pomerantzeff, "Flying spot TV ophthalmoscope," Appl. Opt. **19**(17), 2991-2997 (1980).

[7] M. Rajadhyaksha, R. R. Anderson, and R. H. Webb, "Video-rate confocal scanning laser microscope for imaging human tissues *in vivo*," Appl. Opt. **38**(10), 2105-2115 (1999).

[8] A. Plesch, U. Klingbeil, and J. Bille, "Digital laser scanning fundus camera," Appl. Opt. **26**(8), 1480 (1987).

[9] A. Manivannan, P. F. Sharp, R. P. Phillips, and J. V. Forrester, "Digital fundus imaging using a scanning laser ophthalmoscope," Physiol. Meas. **14**(1), 43-56 (1993).

[10] R. H. Webb, G. W. Hughes, and F. C. Delori, "Confocal scanning laser ophthalmoscope," Appl. Opt. **26**(8), 1492-1499 (1987).

[11] K. Kobayashi, and T. Asakura, "Imaging techniques and applications of the scanning laser ophthalmoscope," Opt. Eng. **34**(3), 717-726 (2005).

[12] A. E. Elsner, S. A. Burns, G. W. Hughes, and R. H. Webb, "Reflectometry with a scanning laser ophthalmoscope," Appl. Opt. **31**(19), 3697-3710 (1992).

[13] D. X. Hammer, R. D. Ferguson, T. E. Ustun, C. E. Bigelow, N. V. Iftimia, and R. H. Webb, "Line-scanning laser ophthalmoscope," J. Biomed. Opt. **11**(4), 041126 (2006).

[14] Y. He, H. Li, J. Lu, G. Shi, and Y. Zhang, Retina imaging by using compact line scanning quasi-confocal ophthalmoscope, Chin. Opt. Lett. **11**(2), 1113 (2013).

[15] K. Im, S. Han, H. Park, D. Kim, and B. Kim, Simple high-speed confocal line-scanning microscope, Opt. Express **13**(13), 51515156 (2005).

[16] N. V. Iftimia, D. X. Hammer, C. E. Bigelow, T. Ustun, J. F. de Boer, and R. D. Ferguson, Hybrid retinal imager using line-scanning laser ophthalmoscopy and spectral domain optical coherence tomography, Opt. Express **14**(26), 1290912914 (2006).

[17] K. V. Vienola, M. Damodaran, B. Braaf, K. A. Vermeer, and J. F. de Boer, "Parallel line scanning

ophthalmoscope for retinal imaging," Opt. Lett. **40**(22), 5335-5338 (2015).

[18] B. Lochocki, A. Gambin, S. Manzanera, E. Irles, E. Tajahuerce, J. Lancis, and P. Artal, "Single pixel camera ophthalmoscope," Optica **3**(10), 1056-1059 (2016).

[19] M. S. Muller, J. J. Green, K. Baskaran, A. W. Ingling, J. L. Clendenon, T. J. Gast, and A. E. Elsner, "Non-mydriatic confocal retinal imaging using a digital light projector," Proc. SPIE. **9376**, 93760E (2015).

[20] E. DeHoog, and J. Schwiegerling, "Optimal parameters for retinal illumination and imaging in fundus cameras," Appl. Opt. **47**(36), 6769-6777 (2008).

[21] International Electrotechnical Commission, Safety of Laser Products Part 1: Equipment Classification and Requirements, (Geneva, Switzerland), IEC-60825-1 (2014).

[22] Y. C. Huang, and J. W. Pan, "High contrast ratio and compact sized prism for DLP projection system," Opt. Express **22**(14), 1701617029 (2014).

[23] V. N. Mahajan, Uniform versus Gaussian beams a comparison of the effects of diffraction, obscuration, and aberrations, J. Opt. Soc. Am. A **3**(4), 470-485 (1986).

[24] F. P. Martial and N. A. Hartell, "Programmable illumination and high-speed, multi-wavelength, confocal microscopy using a digital micromirror," PLoS One **7**(8), 0043942 (2012).

[25] N. Chakrova, R. Heintzmann, B. Rieger and S. Stallinga, "Studying different illumination patterns for resolution improvement in fluorescence microscopy," Opt. Express **23**(24), 31367-31383 (2015).

[26] R. Heintzmann and P. Benedetti, "High-resolution image reconstruction in fluorescence microscopy with patterned excitation," Appl. Opt. **45**(20), 5037-5045 (2006).

[27] W. N. Charman , "Optics of the human eye," in *Visual Optics and Instrumentation,* J. C Dillon, ed. (CRC press, Boca Raton, 1991), pp. 126.

[28] European Machine Vision Association, Standard for Characterization of Image Sensors and Cameras, EMVA Standard 1288, (2016).

[29] A. Weber, A. E. Elsner, M. Miura, S. Kompa, and M. C. Cheney, "Relationship between foveal birefringence and visual acuity in neovascular age-related macular degeneration," Eye, **21**(3), 130-134 (2012).

[30] J. V. Kristjansdottir, S. H. Hardarson, G. H. Halldorsson, R. A. Karlsson, T. S. Eliasdottir, and E. Stefansson, "Retinal oximetry with a scanning laser ophthalmoscope," Invest. Ophthalmol. Vis. Sci. **55**(5), 31203126 (2014).

[31] H. Li, J. Lu, G. Shi, and Y. Zhang, Measurement of oxygen saturation in small retinal vessels with adaptive optics confocal scanning laser ophthalmoscope," J. Biomed. Opt. **16**(11), 110504 (2011).

[32] K. V. Vienola, B. Braaf, C. K. Sheehy, Q. Yang, P. Tiruveedhula, D. W. Arathorn, J. F. de Boer, and A. Roorda, "Real-time eye motion compensation for OCT imaging with tracking SLO," Biomed. Opt. Express **3**(11), 2950-2963 (2012).

[33] C. K. Sheehy, Q. Yang, D. W. Arathorn, P. Tiruveedhula, J. F. de Boer, and A. Roorda, "High-speed, image based eye tracking with a scanning laser ophthalmoscope," Biomed. Opt. Express **3**(10), 2611-2622 (2012).

[34] R. W. Knighton and X. Huang, Linear Birefringence of the Central Human Cornea, Invest. Ophthalmol. Vis. Sci. **43**(1), 8286 (2016).

[35] K. V. Vienola, M. Damodaran, B. Braaf, K. A. Vermeer, and J. F. De Boer, "In vivo retinal imaging for fixational eye motion detection using a high-speed digital micromirror device (DMD)-based ophthalmoscope," Biomed. Opt. Express **9**, 591602 (2018).

[36] M. Damodaran, K. V Vienola, K. A. Vermeer, and J. F. De Boer, "Dual-wavelength Scanning Light Ophthalmoscope with concentric circle scanning," Invest. Ophthalmol. Vis. Sci. 58, 3132 (2017).

[37] S. Martinez-Conde, S. L. Macknik, and D. H. Hubel, The role of fixational eye movements in visual perception, Nat. Rev. Neurosci. **5**(3), 229240 (2004).